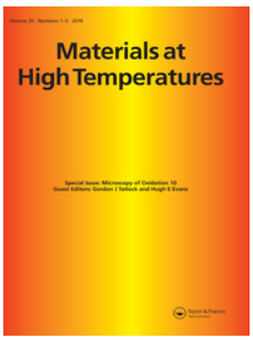

Taylor & Francis
Taylor & Francis Group

Materials at High Temperatures

ISSN: 0960-3409 (Print) 1878-6413 (Online) Journal homepage: http://www.tandfonline.com/loi/ymht20

Stress corrosion of Ni-based superalloys

L. Brooking, J. Sumner, S. Gray & N. J. Simms

To cite this article: L. Brooking, J. Sumner, S. Gray & N. J. Simms (2018) Stress corrosion of Ni-based superalloys, Materials at High Temperatures, 35:1-3, 120-129, DOI: 10.1080/09603409.2017.1392414

To link to this article: https://doi.org/10.1080/09603409.2017.1392414

Published online: 03 Dec 2017.

MATERIALS AT HIGH TEMPERATURES, 2018
VOL. 35, NOS. 1–3, 120–129
https://doi.org/10.1080/09603409.2017.1392414

Taylor & Francis
Taylor & Francis Group

Stress corrosion of Ni-based superalloys

L. Brooking[a], J. Sumner[a], S. Gray[b] and N. J. Simms[a]

[a]Power Engineering Centre, Cranfield University, Cranfield, UK; [b]Surface Engineering & Nanotechnology Institute, Cranfield University, Cranfield, UK

ABSTRACT

The development of gas turbines to increase fuel efficiency is resulting in progressively higher operating temperatures in the under platform regions of the blades. These regions have traditionally been considered low risk areas. However, higher metal temperatures combined with stresses and the deposition of contaminants from the cooling air system may result in complex degradation mechanisms. Static stress corrosion testing has been conducted on C-ring specimens at a range of stresses in a hot corrosion environment. Cracks were observed in C-rings after exposure times greater than 100 h. Scanning electron microscopy (SEM) systems were used to image cracks and characterise deposits to improve understanding of the mechanism. Finite element analysis (FEA) has been used to model the stress intensity under test conditions. CMSX-4 specimens subject to static stresses combined with hot corrosion demonstrated significant material degradation (crack initiation and propagation) suggesting a combined stress corrosion mechanism resulting in cracking.

ARTICLE HISTORY
Received 13 September 2017
Accepted 9 October 2017

KEYWORDS
Stress Corrosion; superalloy; C-ring; FEA

Introduction

Gas turbines are widely used in power generation systems. Developments to improve their efficiencies have led to increased operating temperatures of regions of some components, such as the under platform areas of turbine blades. The high stress state of the root pocket due to the high rotational speeds, combined with cooling air derived deposits and temperatures approaching the conditions associated with type II corrosion, can lead to cracking [1].

CMSX-4 (Table 1) is a single crystal Ni-based superalloy commonly used for 1st stage gas turbine blades as a result of its good high temperature creep-strength properties combined with production affordability [2]. However due to its composition (lower Cr content than other commonly used 1st stage turbine blade materials), CMSX-4 is susceptible to type II hot corrosion. This can result in damage that has the morphology of either pitting or broad fronted attack. Sumner et al. [3] have reported investigations of type II hot corrosion of CMSX-4, using statistical analysis of large data sets to generate models for specific conditions. They observed broad fronted attack and more rapid depletion of Cr in CMSX-4, when compared with IN738LC.

Reaserch conducted on hot corrosion mechanisms in 1970s–80s is summarised by Luthra & LeBlanc [4]. They concluded that hot corrosion could occur through a combination of three mechanisms: sulphidation-oxidation, formation of volatile compounds beneath the protective oxide layer or scale fluxing. Fluxing models have since gained the widest acceptance for deposit induced hot corrosion [5,6].

The process of type II hot corrosion of Ni-based superalloys requires the formation of a liquid eutectic film [5,6]. Type II hot corrosion occurs in the temperature range of 650–800 °C through the formation of minimum melting point mixtures of Na_2SO_4, $NiSO_4$ and $CoSO_4$ [4,5,8]. $NiSO_4$ and $CoSO_4$ compounds form as a result of the reaction of SO_3 with nickel and cobalt from the superalloy. A widely accepted mechanism for hot corrosion was proposed by Goebel & Pettit [9]. Their mechanism outlines two stages, firstly the incubation stage, where a liquid eutectic of Na_2SO_4, $NiSO_4$ and/or $CoSO_4$ forms on the component surface as a result of deposition coupled with a reaction between sulphur oxides and nickel and/or cobalt from the superalloy. The second stage is the propagation stage, where the fluxing of the surface oxide by a liquid deposit on the surface allows inward access, and outward Co/Ni transport. This form of attack often results in pitting damage with an outer NiO/CoO layer being formed, although sometimes a form of broad fronted attack develops [5,6].

For type II hot corrosion many researchers have noted the importance of a constant SO_x supply for

CONTACT J. Sumner j.sumner@cranfield.ac.uk

Table 1. Composition of CMSX-4 (wt%).

Alloy	Cr	Co	Mo	Al	Ti	Ta	Re	Hf	Ni
CMSX-4	6·5	9·6	0·6	5·6	1·0	6·5	3·0	0·1	Bal.

sustained corrosion to occur [3,7,9,10]; this variation of the damage mechanism is known as gas induced acidic fluxing [8,11]. Without both gaseous SO_x and a regular sulphate deposition flux, the corrosion reaction would cease to occur when all the reactants have been consumed.

Type II hot corrosion combined with static stress in Ni-based superalloys has not been extensively studied. However, stress corrosion cracking (SCC) is a well-documented failure mechanism especially in aqueous systems [12,13].

Studies have been conducted on the effects of stress on corrosion pitting growth in aluminium alloys [14]. It was found that corrosion pit growth could be affected by time, stress amplitude and frequency in a fatigue environment. The methodology of Ishihara et al. [14] was applied to Ni-based superalloys by Chan et al. [15]. They considered the point at which fatigue crack growth exceeds corrosion pit growth. However, neither of these studies consider the effect of hot corrosion on the materials stress intensity threshold (k_{th}), the threshold below which cracking does not occur.

Finite element analysis (FEA) is a commonly used method to calculate stresses within complex geometries or multiaxial loading states. This is done by meshing the geometry as a net of elements and nodes. The elements can deform as constrained by the material model, whereas the load is transferred from element to element through the node connections. FEA has been widely used to assess the stress in statically and cyclically loaded conditions.

Experimental method

C-ring test method

C-ring specimens were manufactured from CMSX-4 bars. Guidelines for the dimensions were taken from ISO 7539-5 [16]. The final dimensions for the specimens used in this testing are given in Figure 1. C-ring specimens where manufactured with a < 001 > crystallographic orientation aligned with the cylinder axis.

For target stress levels at a constant stain, the required displacement of the C-rings were calculated by first calculating the change in diameter (ΔD) required to achieve a given stress (Equation (1)).

Equation (1): Change in diameter from ISO 7539-5 [16].

$$\Delta D = \sigma \pi d^2 / 4EtZ \tag{1}$$

FEA modelling was used to verify the stress calculations. Surrogate data from Siebörger et al. [17] for CMSX-4 provided the Young's modulus (E) for Equation (2) and the monotonic material properties used in FEA modelling. The final stressed diameters (D_f) were calculated using Equation (2):

$$D_f = D_{AV} - \Delta D \tag{2}$$

The C-rings were clamped to the final diameter (D_f) using A2 grade stainless steel M5 nuts, bolts and washers, and measured using a digital micrometre with a resolution of 1 μm (and accuracy of 2 μm). An average of five readings was used to determine the initial external diameter (D_{AV}) from which the final stressed diameter is calculated. These are given in Table 2.

Prior to testing, C-ring samples were cleaned in an ultrasonic bath with IPA (isopropyl alcohol). Corrosion exposures were carried out in a horizontal, controlled atmosphere furnace. The corrosion environment, deposit composition and deposit flux were controlled using the well-established deposit recoat methodology (e.g. Sumner et al. [3]). Specimens were coated with an 80/20 M mixture of Na_2SO_4/K_2SO_4. The mass of deposited salt was measured per unit area and specimens were recoated every 100 h in order to control the deposition flux. A gaseous environment of air – 300 vppm SO_2 was used, and all testing was conducted at 550 °C. C-rings were stressed to 800, 700 and 500 MPa, and exposed for 100, 300 or 500 h exposure times with a target deposition flux of 5 μg/cm^2/h. In addition, one C-ring at each target stress level was exposed for 300 h without any deposit.

Microscopy and analytical methods

Samples were mounted in a 50:50 mixture of MetPrep's epoxy set resin and ballotini (40–70 μm diameter glass spheres). Samples were then sectioned, using oil lubricant to prevent dissolution of corrosion products and deposits, before being ground and then polished to a 1 μm diamond paste finish (again using oil lubricant).

Both optical and SEM examinations of the samples were carried out. Optical microscopy was used to determine if cracking was present in the C-rings after each exposure period. SEM was used to characterise the results of the degradation mechanism's interaction with the alloy microstructure. FEI XL-30 and a JEOL 7800F field electron gun (FEG) SEMs equipped with backscatter energy-dispersive X-ray (EDX) detectors were used for characterisation and SEM imaging. SEM images were post-processed using Image J software to enable accurate measurement of features.

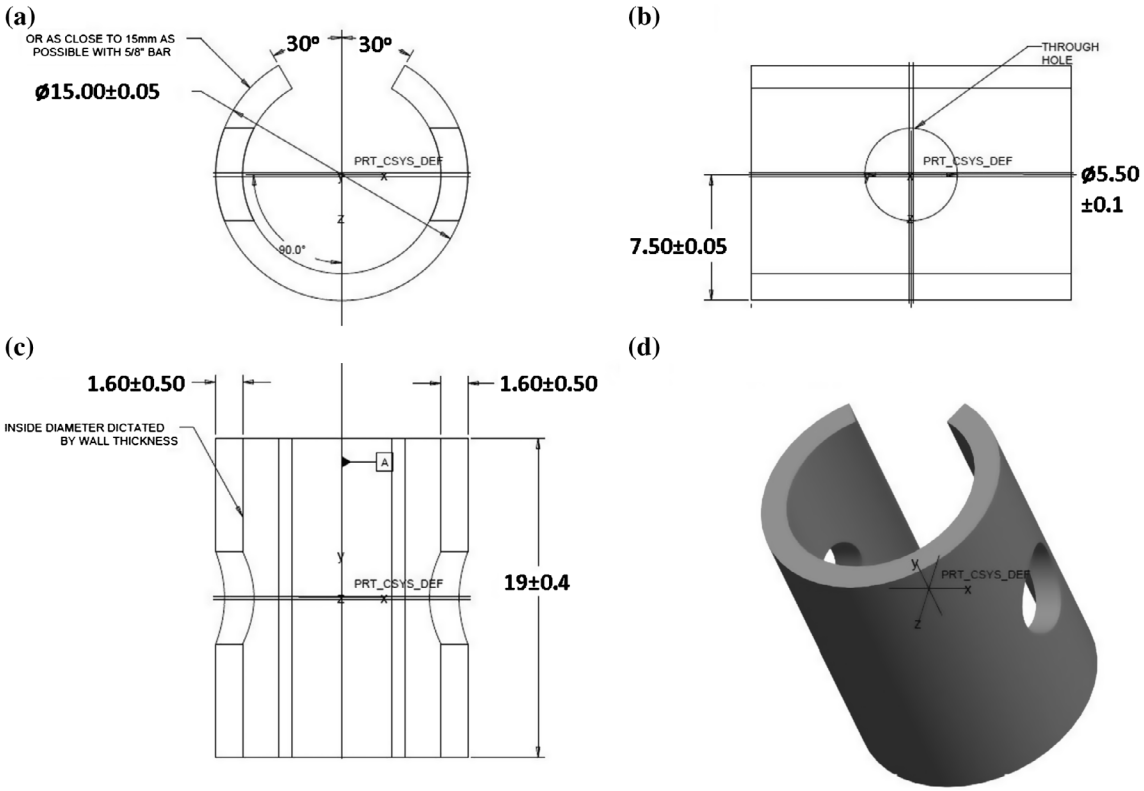

Figure 1. C-ring specimen geometry as established from ISO 7539-5 (a) frontal cross section (b) top view cross section (c) side view cross section (d) isometric view. (Units in mm.)

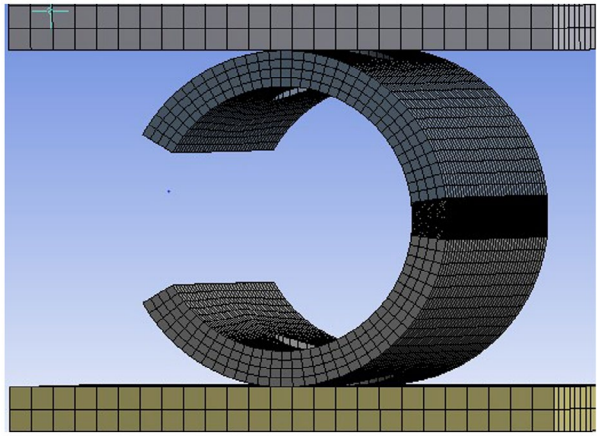

Figure 2. Example of a C-ring mesh constrained between two plates.

FEA analytical methods

FEA modelling was conducted using ANSYS Workbench 15 [18]. The material model used for this analysis was an isotropic model generated using monotonic surrogate material data for CMSX-4 from Siebörger et al. [17]. The C-ring was constrained between two plates (Figure 2). A frictionless sliding contact was utilised between one of the two blocks and the C-ring in order to allow a small amount of relative movement. The boundary conditions were applied through a displacement equivalent to those calculated using Equation (1) (and listed in Table 3).

The C-ring was modelled as three separate sections to allow more accurate refinement of the mesh in the central section of the C-ring. This was important as it was in this central region that it was anticipated that cracking could occur. A hex dominant mesh is used wherever possible; however meshing around the crack tips required the use of a tetrahedral mesh due to the size and complexity of the crack tip geometry.

When clamped, a multiaxial stress condition was predicted in the C-ring. As such the von Mises criterion was used to obtain local stress values. However it was also useful to consider the principal or normal stresses in relation to a mode I crack opening, as shown in Figure 3, as these stresses could be higher for the C-ring geometry in the principal x-axis plane when compared with the von Mises stress.

Linear elastic fracture mechanics (Equation (3)) were used to assess the local stress intensity range (Δk) for micro semi-elliptical cracks within the C-ring. The stress intensity was assessed using the ANSYS R15 [18]

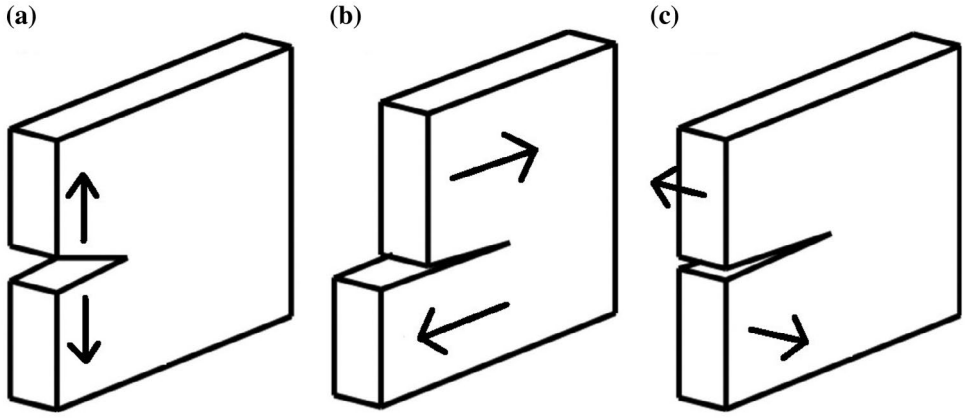

Figure 3. Crack opening modes (a) mode I (b) mode II and (c) mode III.

stress intensity solver code. ANSYS uses T-stress evaluation [19] in order calculate the local crack tip stress intensity.

Equation (3): Linear Elastic Fracture Mechanics Equation [20].

$$\Delta k = \Upsilon \sigma \sqrt{\pi a} \tag{3}$$

FEA generated local crack tip stress intensity predictions were then used to calculate the geometry factor (Υ) for finite surface cracks in the C-ring geometry. Δk can then be compared to k_{th} to assess the likelihood of cracking. The k_{th} of CMSX-4 has been reported to be 15 MPa.m$^{1/2}$ in air at 750 °C [21]. Stress intensities _calculated through FEA modelling can be compared to this in order to determine the likelihood of cracking and the effect of hot corrosion on k_{th}.

Results and discussion

C-ring results & discussion

Unstressed sections of CMSX-4 C-rings were corroded at 550 °C with a target deposition flux of 5 µg/cm^2/h and a gaseous environment of air – 300 vppm SO_2. Samples were removed after exposure times of 100, 300 and 500 h. Inspection showed formation of an oxide scale containing Co, Ni, S and O (Figure 4 and 5). Sulphidation had occurred beneath the oxide scale, consistent with type II hot corrosion [7,22].

For stressed C-rings, cracking of corroded samples was observed at 800 and 700 MPa after exposures for 100 h; with visible cracking still occurring at 500 MPa for exposure times longer than 100 h (Table 2). By contrast C-ring tests without deposit showed no signs of cracking after 500 h of exposure to the test conditions.

C-rings normally experienced cracking within the most highly stressed central region. However when cracks initiated off centre, cracking would occur either side of the centre line due to the shifted stress distribution around the C-Ring (Figure 6).

The corrosion mechanism varied from attacking the gamma-prime (γ') to attacking the gamma-matrix (γ) This is visible in SEM backscattered imaging as a shift in the contrast between the two microstructural features (Figure 7). This reduction in back scattered electrons is attributable to the lower atomic number of the S and O present in the corrosion products.

SEM imaging suggests that the initial combined presence of stress and hot corrosion results in the reaction of the γ' precipitates. Cracks then initiate from features similar to corrosion pit features (Figure 7) and propagate through the γ' where corrosion is present (Figure 8). Using the results of EDX analysis (Figure 5) it is hypothesised that this is because of the lower Cr and Co content of the γ' precipitates.

Table 2. C-ring visible cracking results.

Stress (MPa)	Exposure (Hours)	Final flux (µg/cm^2/hr)	Cracking observed	Average diameter	Stressed diameter
800	500	5·1	Yes	15·02	14·40
800	300	5·1	Yes	15·01	14·39
800	300	0·0	No	15·03	14·40
800	100	5·0	Yes	15·02	14·40
700	500	5·2	Yes	15·01	14·47
700	300	4·7	Yes	15·05	14·50
700	300	0·0	No	15·01	14·47
700	100	5·2	Yes	14·99	14·46
500	300	0·0	No	15·03	14·64
500	100	5·0	No	14·98	14·59
500	300	5·0	Yes	15·02	14·63
500	500	5·2	Yes	15·02	14·63

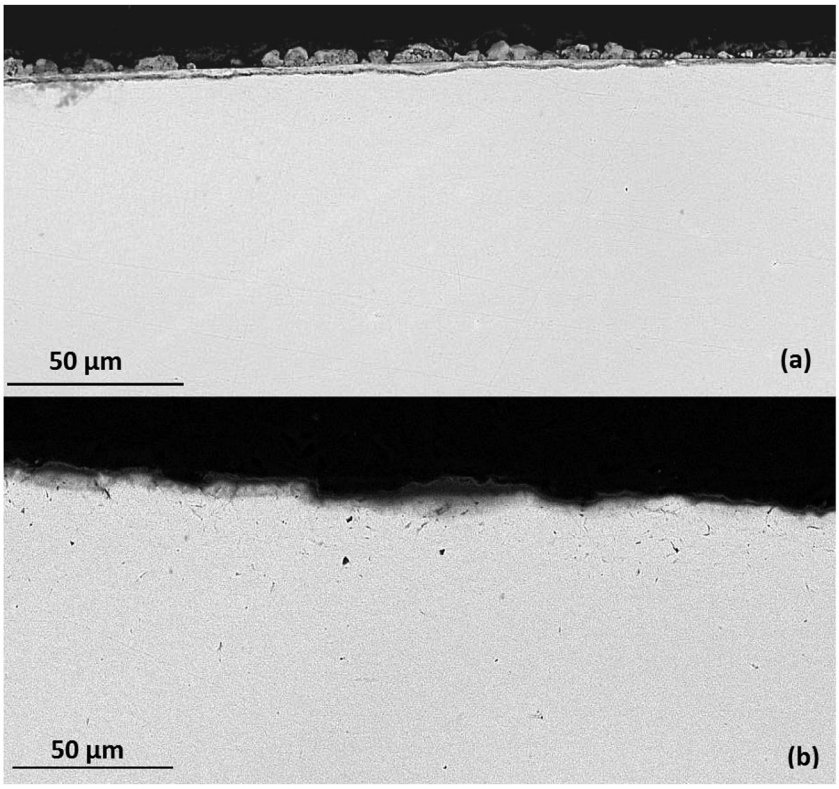

Figure 4. Unstressed corrosion product at 550 °C and exposed to 5 µg/cm^2/h with a test gas of air – 300 vppm SO_2 (a) 500 h resulting in 7·7 µm oxide scale (b) 100 h exposure resulting in 2·43 µm oxide scale.

The corrosion attack shifts to the γ, and it is hypothesised that this happens when the protective NiO/CoO rich oxide scale is formed, as this depletes Co from the alloy which is mainly concentrated in the matrix.

FEA principal and von Mises stress state modelling in C-rings

FEA modelling predicted that maximum stress occurred in the central region of the C-ring as shown in Figure 9. FEA also predicted the presence of a multi-axial stress state within the C-ring, where the largest resolved principal stress plane, referred to as maximum principal, occurs along the x-axis, and the second largest resolved stress plane, referred to as middle principal, occurs in along the z-axis. This stress state would suggest cracks would firstly initiate and then propagate in the z-axis where the maximum principal is acting at a normal in mode I crack opening. However as cracks propagate and Δk exceeds k_{th} then secondary cracks could propagate in all three principle directions. A summary of the stress conditions for various ΔD values is given in Table 3.

FEA was further used to predict the stress intensity and concentration around a crack tip (Figure 10) within the C-ring geometry. These micro-cracks were modelled in the central region of the C-ring using a refined tetrahedral mesh; the results are presented in Table 4.

FEA stress intensity modelling suggests that cracks or pits need to be greater than 100 µm for cracking to occur given a k_{th} of 15 MPa.m$^{1/2}$ as the reported fatigue

Table 3. Calculated stress conditions from ISO 7539–5 and FEA modelling stress results.

Required pre stress (MPa)	ΔD Calculated using ISO 7539–5 (µm)	FEA Maximum von Mises stress (MPa)	FEA maximum principle crack opening stress (MPa)
800	621·0	815	930
700	544·0	712	814
600	466·0	611	693
500	388·0	508	580

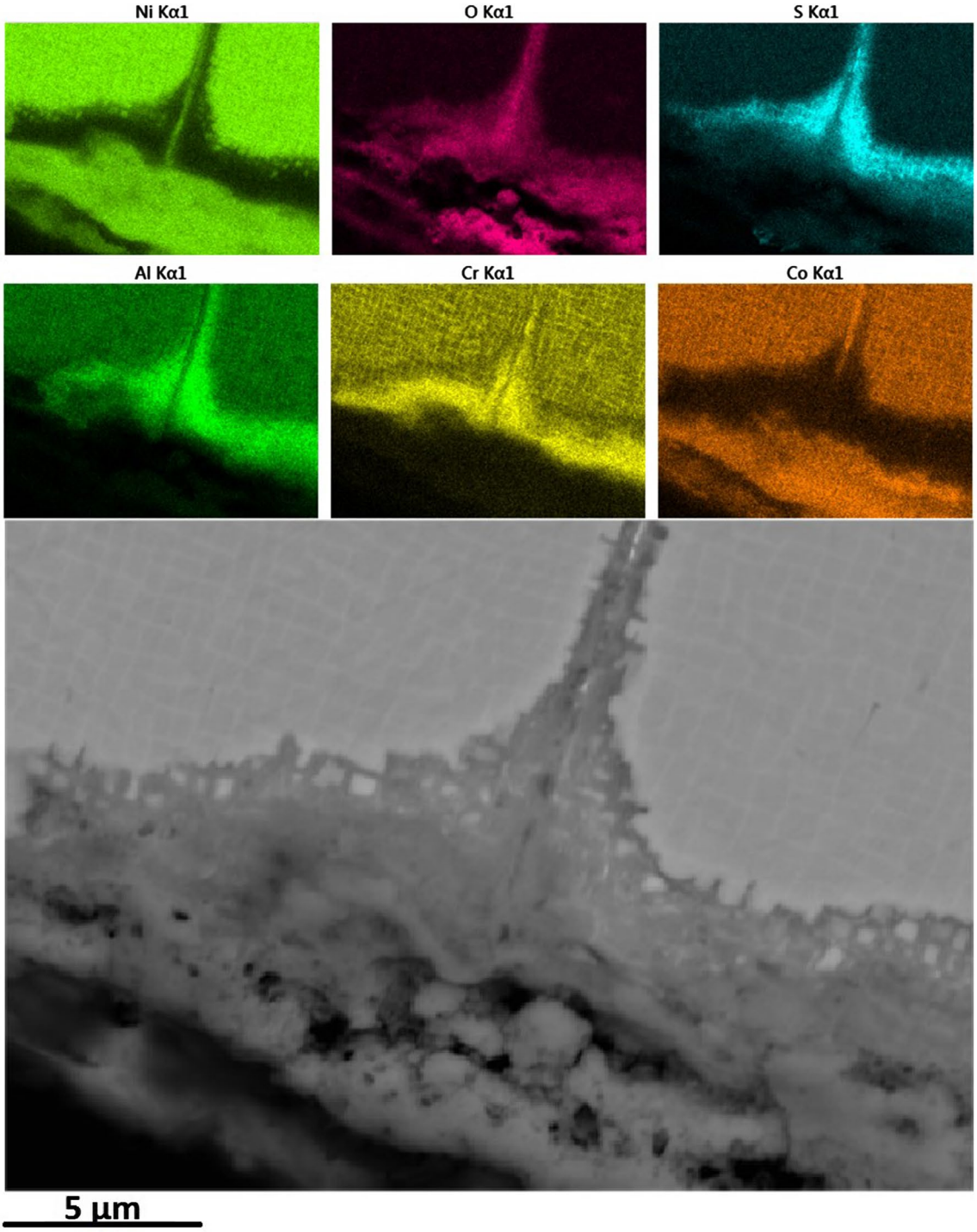

Figure 5. Surface corrosion fatigue crack and back scattered EDX characterisation at 800 MPa after 300 h with a 5 µg/cm^2/h deposition flux and a test gas of air – 300 vppm SO_2.

Table 4. Stress intensity FEA results.

von Mises Stress (MPa)	Crack length (µm)	Peak mode I stress intensity Δk (MPa.m$^{1/2}$)	Calculated geometry factor ε
890	50	9·28	0·832
890	100	13·11	0·831
500	1	0·74	0·837
500	50	5·27	0·841
500	100	7·44	0·839

threshold for CMSX-4 [21]. Therefore the presence of hot corrosion may have a significant effect on reducing the material's k_{th} as well as concentrating stress through corrosion pitting.

Analysis of a corrosion pit's size in cracked C-ring specimen implies that a 10 µm diameter pit has initiated cracking during these exposures (Figure 7). Using

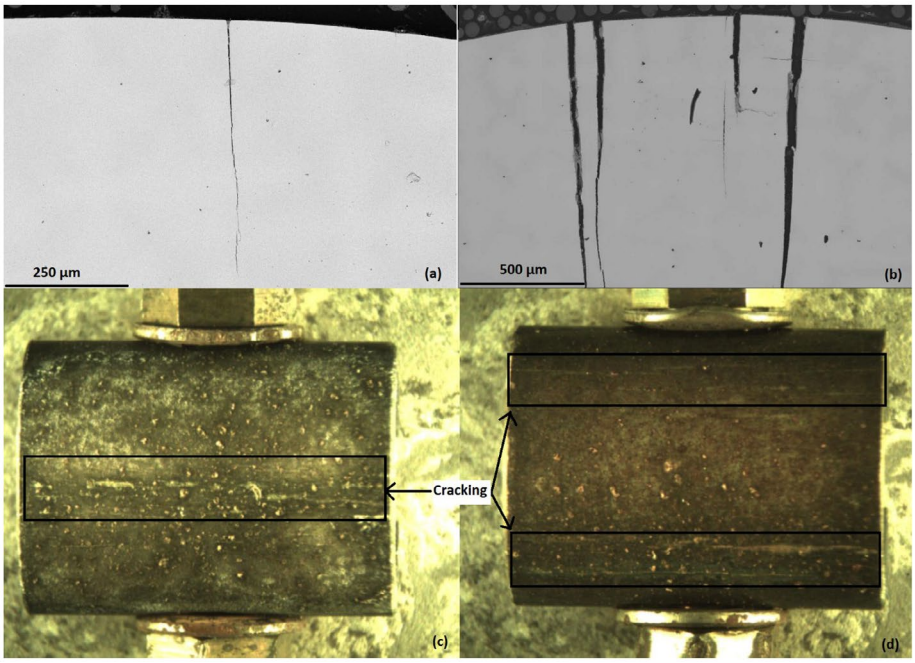

Figure 6. Cracking of C-rings at 800 MPa with a 5 µg/cm^2/h deposition flux and a test gas of air – 300 vppm SO_2 (a) 100 h exposure cross section (b) 300 h exposure cross section (c) 300 h central cracking (d) 500 h symmetrical cracking.

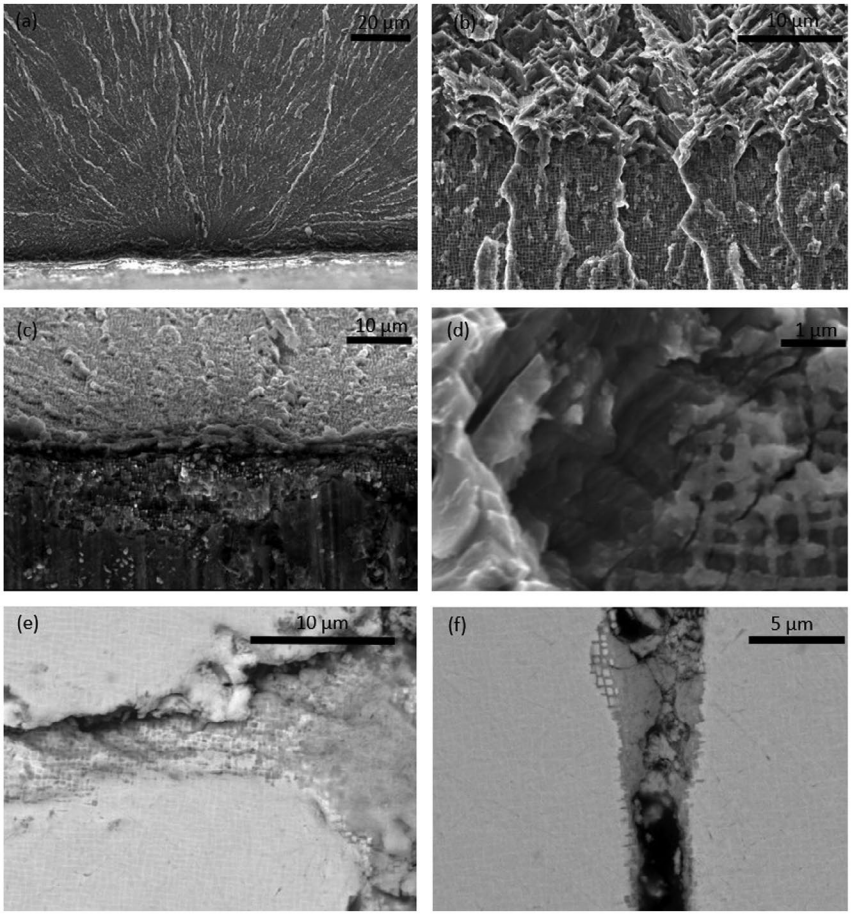

Figure 7. Secondary electron images of 800 MPa C-ring with a 5 µg/cm^2/h deposition flux and a test gas of air – 300 vppm SO_2 (a) 100 h fracture face showing signs of beaching marks (b) 100 h fracture face, crack tip showing attack of γ' (c) 100 h specimen surface showing attack of γ (d) 100 h high mag fracture surface at crack tip (e) 300 h corrosion attack of γ' precipitate (f) 500 h corrosion attack of γ matrix.

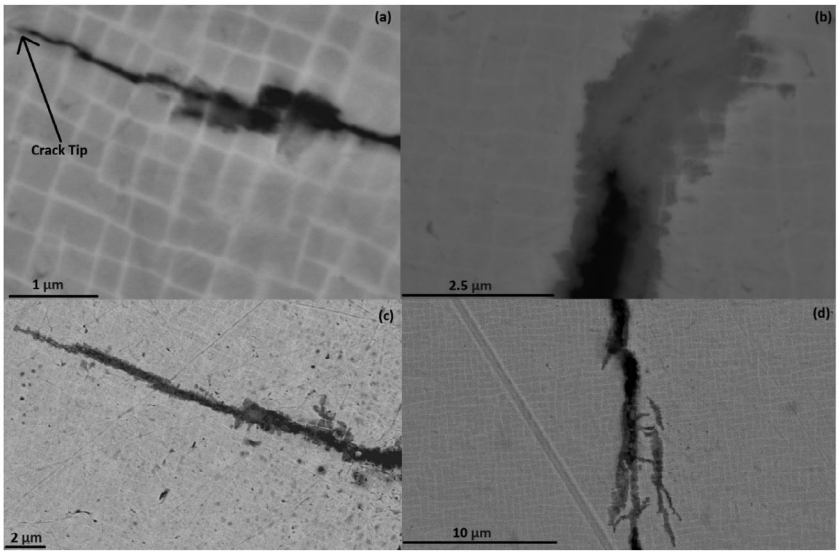

Figure 8. SEM images near crack tips from CMSX-4 C-ring samples stressed to 800 MPa and exposed to a corrosion environment with a deposit flux of 5 µg/cm^2/h and test gas of air – 300 vppm SO_2 (a) 300 h exposure (b) 300 h exposure (c) 300 h exposure (d) 100 h exposure.

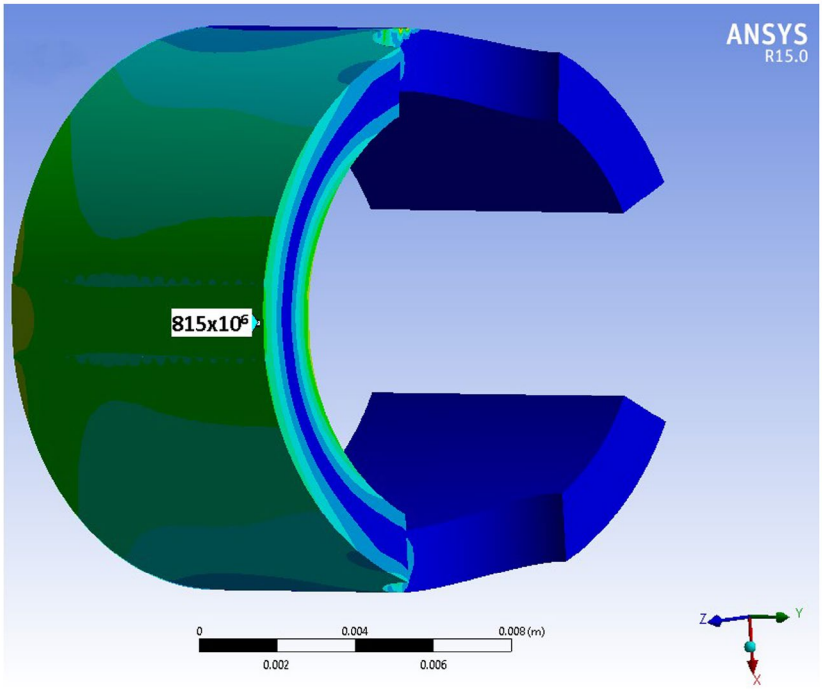

Figure 9. Axis orientation for C-ring modelling, showing normal stress distribution within a C-ring in the principal x-axis, for a boundary condition of $\Delta D = 0{\cdot}612$ mm.

the FEA calculated geometry factor Υ of 0·836, this gives a theoretical reduced k_{th} of 3·748 MPa.m$^{1/2}$ when hot corrosion is simultaneously acting with a stress of 800 MPa; a 75% reduction. This means that cracking can occur at considerably lower applied stresses.

A Kitagawa diagram [23] has been plotted to demonstrate the stress and crack or defect size needed to exceed the material's k_{th} (Figure 11). This is done both for the calculated theoretical k_{th} in hot corrosive conditions, and using the reported k_{th} for air.

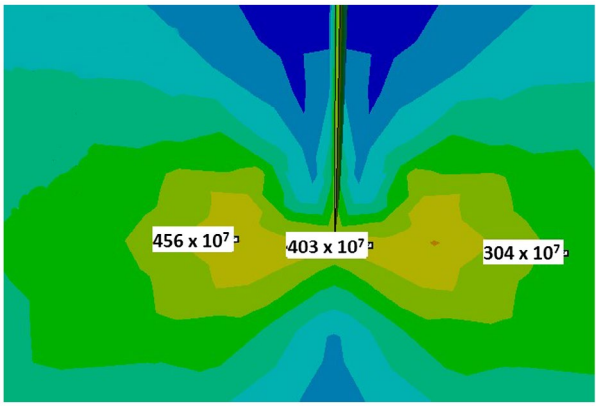

Figure 10. Stress distribution around a centrally located 100 µm crack tip in a C-ring at 890 MPa.

von Mises criterion, FEA calculated equivalent stress concurs with that from ISO 7539-5.

FEA stress intensity modelling around crack tips estimates that fatigue/fracture (k_{th}) can be reduced by up to 75% with the combined effect of hot corrosion in CMSX-4.

SEM imaging suggests the combined hot corrosion stress mechanism initially attacks γ' precipitates, cracks then propagate through precipitates as the mechanism attacks features ahead of its propagation path. A switch to attack of the γ matrix is observed. It is hypothesised that this occurs in order to form the NiO/CoO oxide scale which depletes Co from the γ matrix.

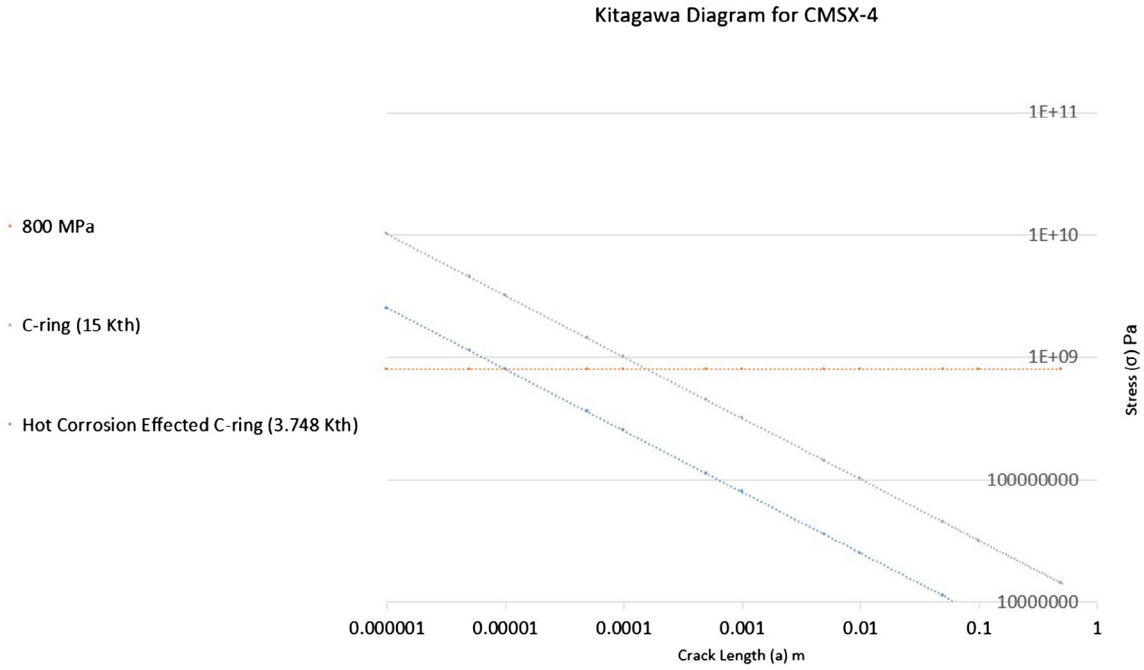

Figure 11. Kitagawa diagram produced from FEA corrosion crack stress intensity analysis, showing the crack defect size required to initiate cracking both with and without the presence of hot corrosion.

Conclusions

SEM/EDX characterisation of the corrosion product produced by stress corrosion in CMSX-4 C-rings at 550 °C is consistent with type II hot corrosion.

Hot corrosion conditions at 550 °C combined with static stresses of greater than 500 MPa can cause a significant hot corrosion stress cracking mechanism. A lower limit seems to exist around 500 MPa. However at exposures greater than 100 h with a flux of 5 µg/cm²/h cracking is still visibly present.

FEA modelling predicts the multiaxial nature of the stress state within a clamped C-ring and the observed cracking in experimental testing supports the modelling results. By determining the effective stress through the

List of symbols

D	Outside diameter
D_f	Final outside diameter when stressed
D_{AV}	Average Diameter of C-ring
σ	Stress
t	C-ring thickness
Z	Correction factor for curved beams
E	Young's modulus
d	Mean inner diameter of C-ring
k	Stress intensity
Υ	LEFM geometry factor
a	Crack length
k_{th}	Stress intensity threshold

Acknowledgements

The authors acknowledge the support of the Engineering and Physical Research Council (EPSRC) for their support for the project - Flexible and Efficient Power Plant: Flex-E-Plant (grant number: EP/K021095/1). They also thank the following partners for their the valuable contributions: GE Energy, Doosan Babcock Limited, Centrica plc., EDF Energy (West Burton Power) Limited., Uniper Technology Limited, Goodwin Steel Castings Limited, NPL Management Limited, R-MC Power Recovery Limited., RWE Generation UK plc., Scottish and Southern Energy (SSE) plc., Siemens Industrial Turbomachinery, and TWI Limited.

Disclosure statement

No potential conflict of interest was reported by the authors.

Funding

This work was supported by Engineering and Physical Research Council (EPSRC) [grant number EP/K021095/1].

References

[1] Rahman MM, Ibrahim TK, Abdalla AN. Thermodynamic performance analysis of gas-turbine power-plant. Phys Sci. 2011;6(14):3539–3550.
[2] Harris K, Wahl JB. Improved single crystal superalloys, CMSX-4 (SLS) [La+Y] and CMSX-486. Superalloys 2004 (Tenth Int Symp). 2004; No. Figure 1:45–52.
[3] Sumner J, Encinas-Oropesa A, Simms N, Nicholls JR. Type II hot corrosion: behaviour of CMSX-4 and IN738LC as a function of corrosion environment. Mater Corros. 2014;65:188–196.
[4] Luthra KL, Leblanc OH. Low temperature hot corrosion of Co-Cr-AI alloys*. Mater Sci Eng. 1987;87:329–335.
[5] Birks N, Meier GH, Pettit FS. High-temperature corrosion resistance. JOM. 1987;39(12):28–31.
[6] Nicholls JR, Simms NJ. Gas turbine oxidation and corrosion, in. Shreir's Corrosion. 2010;518–540.
[7] Young D. High temperature oxidation and corrosion of metals, in. Elsevier Corrosion Series. 2015;1:576.
[8] Eliaz N, Shemesh G, Latanision RM. Hot corrosion in gas turbine components. Eng Fail Anal. 2002;9(1):31–43.
[9] Goebel JA, Pettit FS. Na2SO4-induced accelerated oxidation (hot corrosion) of nickel. Metall Trans. 1970;1(7):1943–1954.
[10] Lortrakul P, Trice RW, Trumble KP, Dayananda MA. Investigation of the mechanisms of Type-II hot corrosion of superalloy CMSX-4. Corros Sci. 2014;80:408–415.
[11] Luthra KL, Begman PA, Wortman DJ, Fryxell RE. Mechanism of low temperature hot corrosion: burner rig studies. Thin Solid Films. 1979;64:281–288.
[12] Zadorozne NS, Giordano MC, Ares AE, Carranza RM, Rebak RB. Anodic characteristics and stress corrosion cracking behavior of nickel rich alloys in bicarbonate and buffer solutions. Corros Sci. 2016;108:1–10.
[13] Chopra OK, Soppet WK, Shack WJ. Effects of alloy chemistry, cold work, and water chemistry on corrosion fatigue and stress corrosion cracking of nickel alloys and welds. Corrosion. 2001:50.
[14] Ishihara S, Saka S, Nan ZY, Goshima T, Sunada S. Prediction of corrosion fatigue lives of aluminium alloy on the basis of corrosion pit growth law. Fatigue Fract Eng Mater Struct. 2006;29(6):472–480.
[15] Chan KS, Enright MP, Moody JP. Development of a probabilistic methodology for predicting hot corrosion fatigue crack growth life of gas turbine engine disks. J Eng Gas Turbines Power. 2014;136(2):22505.
[16] ISO 7539-5. Corrosion of metals and alloys – Stress corrosion testing – Part 5: preparation and use of C-ring specimens. No. 1, 1989.
[17] Siebörger D, Knake H, Glatzel U. Temperature dependence of the elastic moduli of the nickel-base superalloy CMSX-4 and its isolated phases. Mater Sci Eng A. 2001;298(1–2):26–33.
[18] ANSYS Workbench 15.0. ANSYS, 2013.
[19] Gupta M, Alderliesten RC, Benedictus R. A review of T-stress and its effects in fracture mechanics. Eng Fract Mech. 2015;134:218–241.
[20] Dowling NE. Mechanical behavior of materials. 4th ed. Boston, MA: Pearson; 2012.
[21] Joyce MR, Wu X, Reed PAS. The effect of environment and orientation on fatigue crack growth behaviour of CMSX-4 nickel base single crystal at 650 °C. *Mater Lett*. 2004;58(1–2):99–103.
[22] Bird RB, Stewart WE, Lightfoot EN. Transport Phenomena. New York, (NY): Wiley; 2007.
[23] Maierhofer J, Gänser HP, Pippan R. Modified Kitagawa-Takahashi diagram accounting for finite notch depths. Int J Fatigue. 2015;70:503–509.

Stress corrosion of Ni-based superalloys

Brooking, Laurie

2017-12-03

Brooking L, Sumner J, Gray S, Simms N. (2018) Stress corrosion of Ni-based superalloys. Materials at High Temperatures, Volume 35, Issue 1-3, 2018, pp. 120-129
http://dx.doi.org/10.1080/09603409.2017.1392414